Nanoscale

ROYAL SOCIETY OF CHEMISTRY

MINIREVIEW

View Article Online
View Journal | View Issue

Cite this: *Nanoscale*, 2022, **14**, 7957

Recent progress of Bi-based electrocatalysts for electrocatalytic CO_2 reduction

Dong Xia,†[a] Huayang Yu,†[b] Huan Xie,[c] Peng Huang,[d] Robert Menzel,[e] Maria Magdalena Titirici *[f] and Guoliang Chai *[a]

Received 6th April 2022,
Accepted 12th May 2022

DOI: 10.1039/d2nr01900k

rsc.li/nanoscale

To mitigate excessively accumulated carbon dioxide (CO_2) in the atmosphere and tackle the associated environmental concerns, green and effective approaches are necessary. The electrocatalytic CO_2 reduction reaction (CO_2RR) using sustainable electricity under benign reaction conditions represents a viable way to produce value-added and profitable chemicals. In this minireview, recent studies regarding unary Bi electrocatalysts and binary BiSn electrocatalysts are symmetrically categorized and reviewed, as they disclose high faradaic efficiencies toward the production of formate/formic acid, which has a relatively higher value of up to 0.50 $·per kg and has been widely used in the chemical and pharmaceutical industry. In particular, the preparation methodologies, electrocatalyst morphologies, catalytic performances and the corresponding mechanisms are comprehensively presented. The use of solid-state electrolytes showing high economic prospects for directly obtaining high-purity formic acid is highlighted. Finally, the remaining questions and challenges for CO_2RR exploitations using Bi-related electrocatalysts are proposed, while perspectives and the corresponding strategies aiming to enhance their entire catalytic functionalities and boost their performance are provided.

Introduction

The development of human society to where we are today is linked to the utilization of fossil fuels, which consequently are responsible of the excessive release of carbon dioxide (CO_2) into the atmosphere causing severe environmental concerns.[4–6] As such, reducing and utilizing the released CO_2 in a circular fashion have been recognized internationally as a way forward,[12] to move towards carbon neutrality by 2060.[15] Adopting green and environmentally benign approaches to close the carbon cycle is of paramount importance. Among these, the electrochemical carbon dioxide reduction reaction (CO_2RR) approach is highly promising, as it operates under mild conditions (*e.g.* ambient temperature and pressure) using renewable energy and generates different products by simply alternating the catalytic conditions (*e.g.* electrolytes, electrocatalysts, configurations of electrolytic cells, and reduction potentials).[19–21] Additionally, CO_2 as an electrochemical precursor can generate various high-value products and chemicals, such as carbon monoxide (CO),[22,23] methane (CH_4),[25,26] formic acid (HCOOH) or formate ($HCOO^-$),[27,28] methanol (CH_3OH),[29,30] ethylene (C_2H_4),[31,32] ethanol (CH_3CH_2OH),[34,35] and *n*-propanol (*n*-C_3H_7OH).[37,38] Among these carbon-containing products, HCOOH/$HCOO^-$ exhibits a high net present value by techno-economic assessments[12,43] and is useful and widely needed in the areas of producing chemicals and pharmaceuticals, supplying protons in proton-exchange membrane fuel cells, and functioning as an important hydrogen carrier.[44–46]

Numerous types of electrocatalysts display promising CO_2RR performances towards the production of HCOOH/$HCOO^-$ with high faradaic efficiency (FE). Typical examples include bismuth (Bi),[48] tin (Sn),[49] indium (In),[51] cadmium (Cd),[53] lead (Pb),[54] mercury (Hg),[55] *etc.*[56,57] Among these, Bi-based electrocatalysts have attracted great attention, owing to their low costs, non-toxicity and high abundance in nature. Bi possesses a relatively high positive standard reduction potential (Bi^{3+}/Bi, 0.308 V) and thus a high overpotential is required to activate the competitive hydrogen evolution reaction (HER) in CO_2RR experiments.[58,59] Although Sn-based electrocatalysts share similar characteristics to Bi (*e.g.* inexpensiveness, high reserves and environmental benignness),[60] unary Sn electro-

[a]*State Key Laboratory of Structural Chemistry, Fujian Institute of Research on the Structure of Matter, Chinese Academy of Sciences, Fuzhou, Fujian 350002, China. E-mail: g.chai@fjirsm.ac.cn*
[b]*School of Design, University of Leeds, Leeds, LS2 9 JT, UK*
[c]*Jiangsu Co-Innovation Center of Efficient Processing and Utilization of Forest Resources, International Innovation Center for Forest Chemicals and Materials, College of Materials Science and Engineering, Nanjing Forestry University, Nanjing, Jiangsu 210037, China*
[d]*Department of Materials, University of Manchester, Manchester, M13 9PL, UK*
[e]*School of Chemistry, University of Leeds, Leeds, LS2 9 JT, UK*
[f]*Department of Chemical Engineering, Imperial College London, London SW7 2AZ, UK. E-mail: m.titirici@imperial.ac.uk*
†These authors contributed equally.

catalysts generally exhibit a low FE towards $HCOOH/HCOO^-$ and tend to yield large proportions of mixed H_2 and CO gases during the CO_2RR practices, because their different valence states.[59] Their catalytic activity can been modulated either *via* different methodologies or by hybridization with new functional components to acquire a broad spectrum of CO_2RR-associated performances.[62] Density functional theory (DFT) calculations elucidate that the crystalline surfaces of Bi and Sn metals present favorable binding energy towards the *OOCH intermediate, resulting in the final generation of HCOOH or $HCOO^-$ depending on the electrolytes.[62]

Several insightful reviews have been published on the state-of-the-art progress and advancements of various metal-based electrocatalysts for CO_2RR studies, which cover broad metallic categories and multiple electrocatalytic products.[63,64] Recently, Sn-based electrocatalysts have been comprehensively summarized by Zhao *et al.*[62] and An *et al.*,[66] encompassing catalyst synthesis, compositions, morphologies and performances. Bi-Based electrocatalysts for electrochemical CO_2RR applications were summarized by Guan *et al.*,[59] but with no discussions in utilizing solid-state electrolytes for the production of high-purity and concentrated HCOOH from Bi electrocatalysts. Utilizing solid-state electrolytes in the CO_2RR is an emerging research area, which enables attaining concentrated ready-to-collect liquid compounds, thereby waiving the subsequent complex and expensive downstream separation procedures that are required for aqueous electrolytes.[70] On the other hand, reviews of the electrocatalytic CO_2RR with a special focus on the $HCOOH/HCOO^-$ products have rarely been reported.[68] To fill the gaps, this minireview concentrates on recent studies about unary Bi-based electrocatalysts and binary BiSn-related electrocatalysts in the CO_2RR areas.

In this minireview, methodologies for the fabrication of unary Bi-based electrocatalysts and factors influencing their CO_2RR functionalities are presented and special attention has been paid to solid-state electrolytes in four-chamber electrolytic cells. Then, less-frequently reported, structure-varied binary BiSn-based electrocatalysts are summarized and commented on in the following section. Perspectives for further enhancing Bi-based electrocatalyst performances and challenges to reach techno-economic prospects in the future have been proposed, aiming to address their current challenges, advance the developments, and expedite their commercialization. The general information of this minireview is provided in Fig. 1. This minireview is expected to offer guidance and new insights into constructing multitudinous performance-reinforced CO_2RR electrocatalysts for the effective conversion of CO_2 to high-quality fuels and, in turn, to help reduce the carbon footprint.

Unary Bi-based electrocatalysts

Bi-Based electrocatalysts belong to a large category and are a fast-changing subject in the field of the CO_2RR. Detailed reviews with respect to tailoring their surface morphologies, creating defects, dislocations and grain boundaries and tuning compositions and fabricating composites have been reported elsewhere. The latest publications continue to outperform the state-of-the-art findings, which deserve a systematic review and summary for clear understanding and updating on the latest advancements for the academic community, especially newcomers to the field of CO_2 electroreduction. Recent studies on morphology, methodology and technology towards the production of unary Bi-relevant electrocatalysts for formate production in addition to sophisticated configurations of electrolytic cells for direct high-purity formic acid synthesis are reviewed in the section below. Table 1 lists the performances

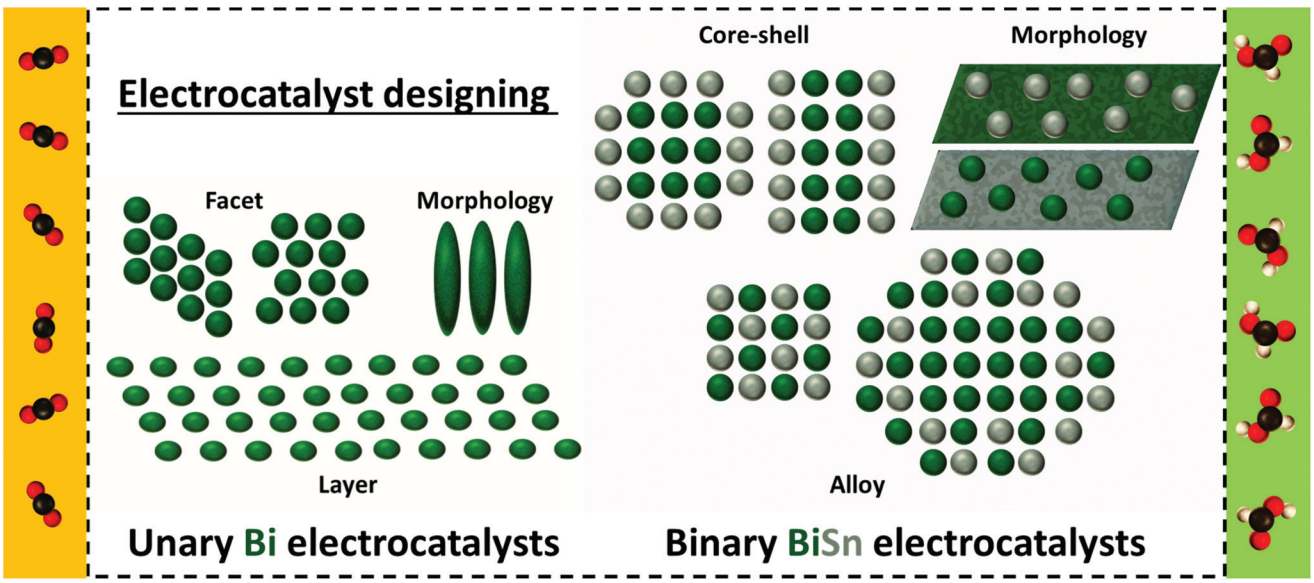

Fig. 1 Schematic illustration of the electrocatalytic CO_2RR to formic acid over various unary Bi electrocatalysts and binary BiSn electrocatalysts.

Table 1 Summary of unary Bi-relevant electrocatalysts for the CO_2RR in aqueous and solid state electrolytes

Electrocatalysts	Synthesis method	Morphology	Electrolyte	Cell	Products	Current density [mA cm^{-2}]	FE (%, *vs.* RHE)	Stability (h)	Ref.
Bi rhombic dodecahedra	Wet chemical reduction	Rhombic dodecahedron	0.5 M $KHCO_3$	H-Type	Formate	~3	93.5% at −0.7 V	10	11
Bi rhombic dodecahedra	Wet chemical reduction	Rhombic dodecahedron	1.0 M KOH	Gas diffusion	Formate	~200	>86% at −0.68 V	20	11
Bi nanostructures	Chemical reduction	Nanostructure	0.5 M $KHCO_3$	H-Type	Formate	~15	92% at −0.9 V	30	33
Bi nanoparticles	*In situ* oxidation–reduction	Nanoparticles	0.5 M $KHCO_3$	H-Type	Formate	6.8	97.4% at −0.78 V	72	41
Bi dendrites	Electrodeposition	Dendrites	0.5 M $KHCO_3$	H-Type	Formate	~3.5	~64% at −0.78 V	—	41
Bismuthene (0.65 nm)	Chemical reduction	Single layer	0.5 M $KHCO_3$	H-Type	Formate	~2.5	98% at −0.58 V	75	9
Bi nanosheets (4.2 nm)	Chemical reduction	Layered nanosheets	0.5 M $KHCO_3$	H-Type	Formate	—	~60% at −0.58 V	—	9
Bi nanosheets (11.33 nm)	Chemical reduction	Layered nanosheets	0.5 M $KHCO_3$	H-Type	Formate	—	~40% at −0.58 V	—	9
Bismuthene	*In situ* electrochemical reduction	Layered nanosheets	1.0 M $KHCO_3$	Gas diffusion	Formate	102.7	~97.4% −1.0 V	25	7
Bismuthene	Galvanic replacement reaction	Layered nanosheets	0.5 M $KHCO_3$	H-Type	Formate	28.7	~94% at −0.80 V	6	36
3D Bi-ene-A/CM	Hydrothermal reaction and electrochemically topotactic conversion.	Bismuthene arrays	1.0 M $KHCO_3$	H-Type	Formate	21.21	96.02% at −0.88 V	12	47
3D Bi-ene-A/CM	Hydrothermal reaction and electrochemically topotactic conversion	Bismuthene arrays	1.0 M KCl/1.0 M $KHCO_3$	Gas diffusion	Formate	~200	93.65%/ 92.57%	12	47
Bismuthene	Templating and electrochemically topotactic conversion	Network morphology with roughened edges	0.5 M $KHCO_3$	H-Type	Formate	~100	~95% at −0.9 V	500	52
Bismuthene	Templating and electrochemically topotactic conversion	Network morphology with roughened edges	1.0 M KOH/1.0 M $KHCO_3$	Gas diffusion	Formate	~200	~95%/>90% at −~0.7 V/−~1.2 V	20/110	52
Bi nanosheets	Electrochemical topotactic reduction	Nanosheets with different oriented angles	0.5 M $NaHCO_3$	H-Type	Formate	24	~100% *vs.* SCE	10	65
Bi nanosheets	Electrochemical conversion	Nanosheet	0.5 M $KHCO_3$	H-Type	Formate	13.3	95% at −0.9 V	15	67
Bi nanosheets	Electrochemical topotactic transformation	Irregular porous nanosheets	0.5 M $KHCO_3$	Gas diffusion	Formate	72	95.2% at −1.4 V	10	69
Bi nanosheets	Hydrothermal reaction and electrochemically topotactic conversion	Hydrangea-like, porous nanostructures	0.5 M $KHCO_3$	H-Type	Formate	~20	~95% at −0.88 V	12	71
Bi nanosheets	Electrochemical exfoliation	Ultrathin nanosheet	0.5 M $KHCO_3$	H-Type	Formate	25	92.5% at −0.97 V	17	3
Bi nanosheets	*In situ* electrochemical transformations	Interconnected nanosheets	0.5 M $KHCO_3$	H-Type	Formate	10.5	92% at −0.9 V	15	13
Bi nanoparticles/ Bi_2O_3 nanosheets	Hydrothermal reduction	Nanoparticles covered nanosheets	0.5 M $NaHCO_3$	H-Type	Formate	24.4	~100% at −0.86 V	>24	16

Table 1 *(Contd.)*

Electrocatalysts	Synthesis method	Morphology	Electrolyte	Cell	Products	Current density [mA cm^{-2}]	FE (%, *vs.* RHE)	Stability (h)	Ref.
Bi/Bi_2O_3 junction nanosheets	*In situ* growth on carbon fiber paper	Curved, interconnected nanosheets with mesopores	0.5 M $KHCO_3$	H-Type	Formate	32.4	90.4% at −0.87 V	31 h, 16 h at −0.67 V, 10 h at −0.77 V and 5 h at −0.87 V	39
Bi nanosheets	*In situ* electrochemical reduction	Crumpled nanosheets	0.5 M $KHCO_3$	H-Type	Formate	21	96.5% at −0.83 V	10 h at −0.83 V	42
Bi nanosheets	*In situ* electrochemical reduction	Crumpled nanosheets	0.5 M $KHCO_3$	H-Type	Formate	17.9	99% at −0.79 V	—	42
Bi nanosheets	*In situ* electrochemical reduction	Crumpled nanosheets	Porous styrene-divinylbenzene copolymer	Customized four-chamber	Formic acid	30	~0.11 M pure formic acid	100	42
Bi nanoparticles	Chemical lithium tuning method	Interconnected nanoparticle networks	Porous styrene-divinylbenzene sulfonated copolymer	Gas diffusion	Formate	~55	97% at −0.77 V	—	50
Bi nanoparticles	Chemical lithium tuning method	Interconnected nanoparticle networks	Porous styrene-divinylbenzene sulfonated copolymer with H_2 flow	Customized four-chamber	Formic acid	30	0.1 M pure formic acid	100	50
Bi nanoparticles	Chemical lithium tuning method	Interconnected nanoparticle networks	Porous styrene-divinylbenzene sulfonated copolymer with N_2 flow	Customized four-chamber	Formic acid	30	~0.35 M pure formic acid vapor	30	50

of the representative literature of unary Bi electrocatalysts for CO_2RR studies.

Bi nanoparticle-based electrocatalysts

Bi-Relevant electrocatalysts have been designed with various facets to enhance the faradaic efficiency (FE) towards the production of formate. Xie *et al.*[11] synthesized Bi rhombic dodecahedra with exposed (104) and (110) facets, as demonstrated by scanning electron microscopy (SEM, Fig. 2a and b) and transmission electron microscopy (TEM, Fig. 2c and d) observations. Measured in an H-type cell for the CO_2RR, the Bi rhombic dodecahedra displayed excellent selectivity for formate in a wide overpotential window (from −0.7 to −1.2 V *vs.* RHE), reaching a maximum FE up to 96.5% at −1.1 V *vs.* RHE (Fig. 2g). The favorable electrocatalytic capability ($FE_{foramte}$ >86%), high operation current density (maintained at around 200 mA cm^{-2}) and structural stability (continuous working of up to 20 h) of the Bi rhombic dodecahedra were further confirmed by experiments in a gas-diffusion flow cell, as shown in Fig. 2h. Density functional theory (DFT) calculations indicated that the well-exposed (104)/(110) facets reflected both lower adsorption free energies of *OCHO and *H intermediates than that of the typical most stable (012) facet (Fig. 2e, Fig. 2f). Interestingly, the adsorption free energy of *OCHO in the CO_2RR was even lower than the corresponding *H in the competitive HER, suggesting that the (104)/(110) surfaces were thermodynamically favorable to adsorb the *OCHO intermediate instead of *H, in line with the excellent electrocatalytic performance of Bi rhombic dodecahedra. However, Lu *et al.*[33] fabricated Bi nanostructure electrocatalysts yielding 92% of formate at −0.9 V *vs.* RHE, which led to an opposite DFT conclusion compared with the Bi rhombic dodecahedra, namely that the adsorption energy of *OCHO on the Bi (012) surface was lower than that of the (104) surface and the (110) surface. A later report regarding exposing the (012) facet of a Bi nanoparticulate electrocatalyst was attempted by Wei *et al.*[41] In the study, the Bi nanoparticles were derived from the electrochemical reduction of carbon cloth supported Bi dendrite precursors, and the Bi dendrites dominated the (003) surface. The prepared Bi nanoparticles were capable of producing 97.4% of formate at −0.78 V *vs.* RHE, while Bi dendrites were only 62% under the same conditions. The DFT calculations demonstrated that the (012) surface showed a lower adsorption free energy of *OCHO than the (003) surface, supporting the above experimental results, *i.e.* Bi nanoparticles were (012) surface abundant and Bi dendrites were (003) surface dominated. These cases clearly disclose the critical importance of manipulating nanoparticles crystalline orientations in affecting electrocatalytic performance, and also signify that the facet plays predominant roles in determining the CO_2RR performance in format-varied, Bi-based electrocatalysts.

Bismuthene-related electrocatalysts

Apart from the facet-varied nanoparticles of Bi-based electrocatalysts, Bi nanosheets also show great prospects in effectively

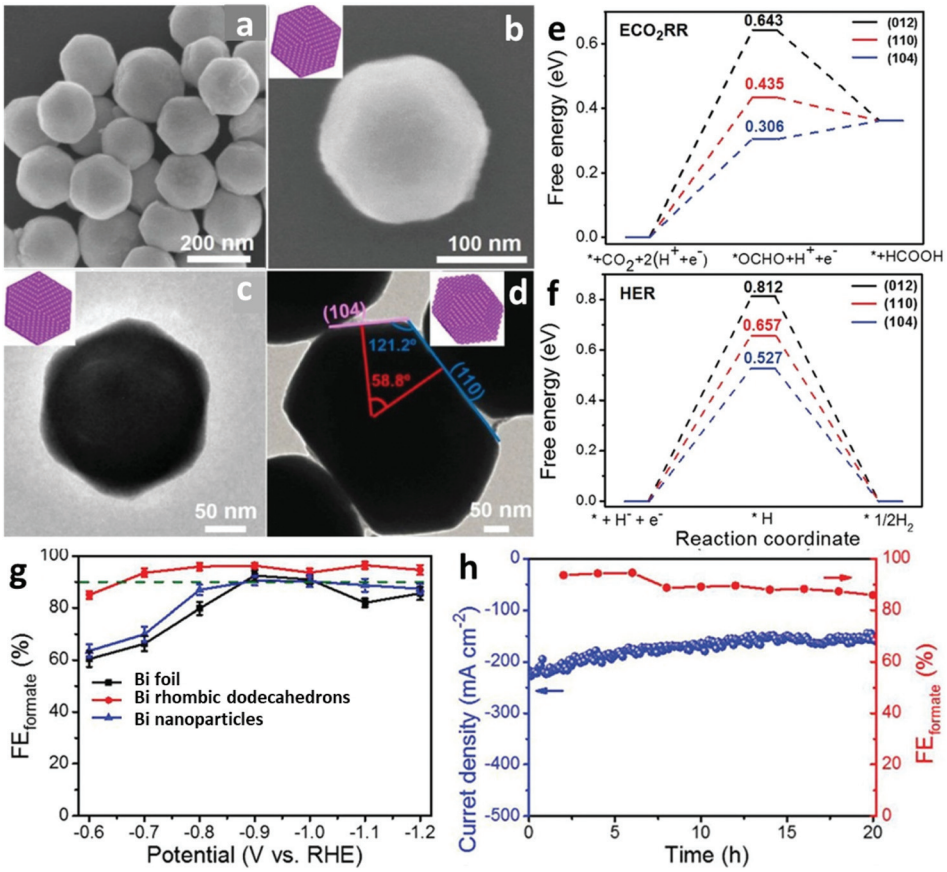

Fig. 2 (a and b) SEM images and (c and d) TEM images of Bi rhombic dodecahedra. (e) Free energy diagrams of the electrocatalytic formation of formate and (f) HER on (012), (110) and (104) facets. (g) Linear sweep voltammetry (LSV) polarization curves of Bi foil, Bi rhombic dodecahedra and Bi nanoparticles in CO_2-saturated 0.5 M $KHCO_3$ solution. (h) Long-electrocatalytic stability and corresponding FE of formate at −0.68 V (*vs.* RHE) measured with a gas-diffusion flow cell with a three-electrode system using 1.0 M KOH.[11] This figure has been adapted from ref. 11 with permission from the John Wiley and Sons, copyright 2021.

converting CO_2 to formate. Amid Bi nanosheets, the two-dimensional monolayer Bi nanosheet, denoted as bismuthene, is considered the most representative, and a couple of methodologies have been successfully adopted to produce it. The first example of bismuthene synthesis was demonstrated by Yang *et al.*,[9] in which a simple wet chemical reduction method was introduced. In detail, bismuthene with the unique exposure of the (111) facet was obtained by adding sodium borohydride solution to reduce bismuth chloride in the presence of 2-ethoxyethanol, followed by ultrasonication to exfoliate the aggregated Bi nanosheets. Several characterization techniques confirmed the successful formation of bismuthene, including the monolayer feature as observed by the TEM image (Fig. 3a), an average height of 0.65 nm as shown by the atomic force microscopy (AFM) image (Fig. 3b and 3c), and a single-atom layer thickness of 0.6 nm with a zig-zag structure as profiled by high-angle annular dark-field scanning transmission electron microscopy (HAADF-STEM, Fig. 3d). The bismuthene exhibited higher catalytic activity (Fig. 3e) than Bi nanosheets, a superior $FE_{formate}$ of up to 98% (Fig. 3f) and also high electrocatalytic stability at a low overpotential of −0.58 V *vs.* RHE (Fig. 3g). The excellent $FE_{formate}$ of bismuthene originated from the lower energy required for OCHO* adsorption than COOH* adsorption and H* adsorption on the (111) surface, as predicted by DFT calculations in Fig. 3h and i. Based on experimental and theoretical calculations, this study highlights the importance of fabricating CO_2RR electrocatalysts with thinner layers to increase the density of active sites and unfold more electroactive facets. Considering the spin–orbit coupling effects, however, the bismuthene displayed lower catalytic activity than the bilayer Bi nanosheet, which was investigated by Wang *et al.* using only DFT calculations.[72] Hence, the bilayer Bi nanosheets working as CO_2RR electrocatalysts can be produced to experimentally verify this theoretical finding, while also filling the gap that no bilayer Bi nanosheet has been implemented for the CO_2RR.

As the distinct CO_2RR capability of bismuthene towards formate production is shown in the above example, more studies concerning the fabrication of bismuthene and investigations of their electrocatalytic performances have been widely exploited. For example, Ma *et al.* employed the *in situ* electrochemical transformation approach to reduce monoclinic

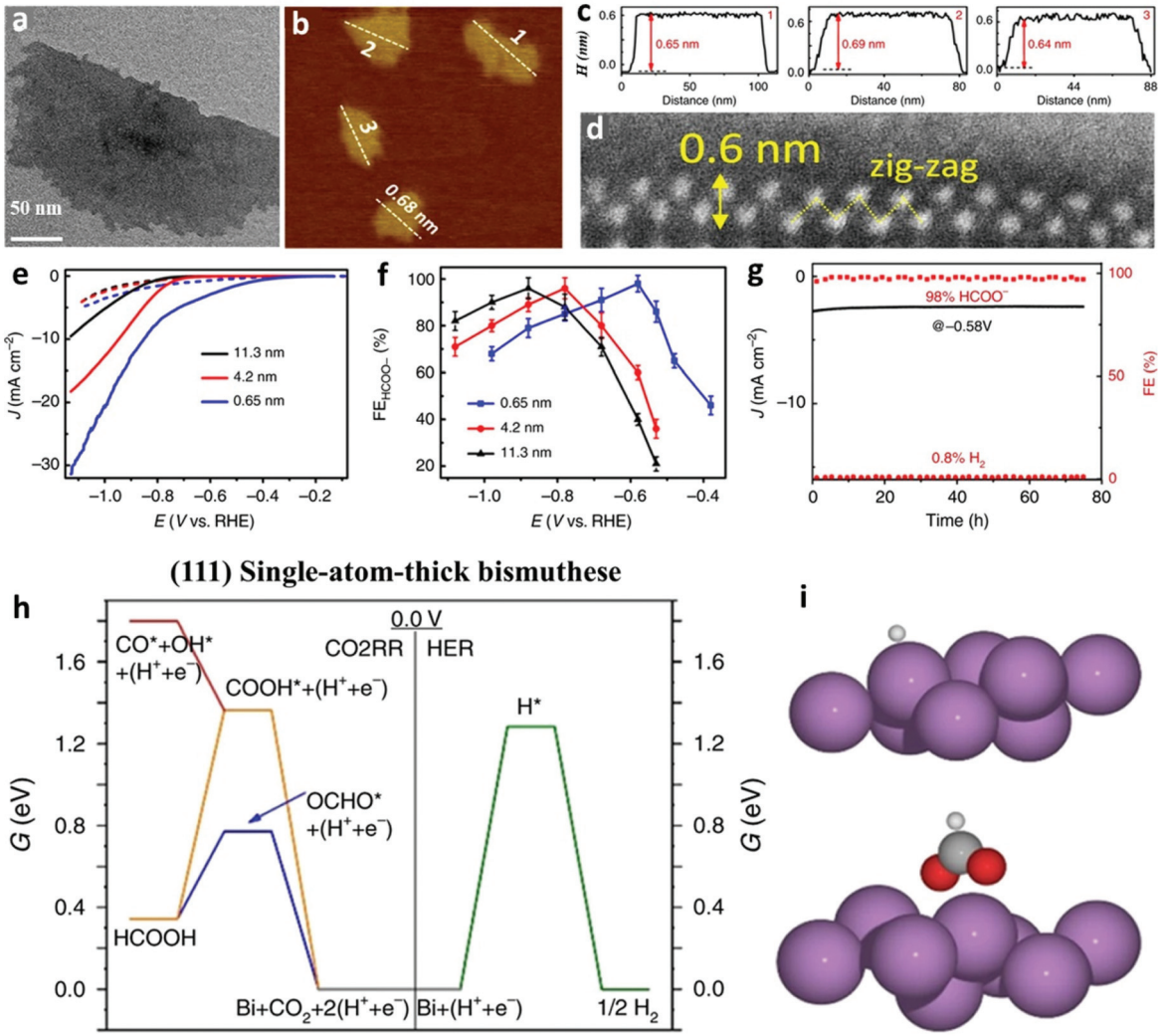

Fig. 3 (a) TEM image of bismuthene. (b) AFM image of bismuthene. (c) The corresponding height profiles of marked bismuthene nanosheets in (b). (d) The lateral HAADF-STEM image of a bismuthene with a zig-zag structure. (e) LSV curves and faradaic efficiencies for formate of thickness-differed Bi nanosheets (bismuthene with a thickness of 0.65 nm) in CO_2 saturated 0.5 M $KHCO_3$ solution. (f) Electrocatalytic performances of Bi nanosheets with different thicknesses. (g) Electrocatalytic stability tests of bismuthene and the corresponding FEs of CO and H_2. (h) Free energy diagrams for the CO_2RR and the HER on (111) single-atom-thick bismuthene. (i) Structural descriptions of OCHO* and H* adsorption onto the Bi (111) surface. Violet, gray, red and white spheres represent respective Bi, C, O and H atoms.[9] This figure has been adapted from ref. 9 with permission from the Springer Nature, copyright 2020.

scheelite bismuth vanadate to ultrathin bismuthene nanosheets at −1.0 V in 1 M $KHCO_3$ solution, in which the ultrathin bismuthene nanosheet had a thickness of ~1.55 nm (Fig. 4a).[7] Owing to the topological transformation, the ultrathin bismuthene nanosheets exhibited a distinct $FE_{foramte}$ selectivity of above 90% at a broad range of overpotential window (−0.65 to −1.4 V *vs.* RHE), with the largest formate selectivity of 97.4% emerged at −1.0 V (*vs.* RHE) accompanied by a current density of −102.7 mA cm^{-2}. Not just limited to flat bismuthene nanosheets, a new form of vertically aligned bismuthene arrays was successfully synthesized using the galvanic replacement reaction, as shown in Fig. 4b.[36] In particular, copper foil as a growth substrate was immersed in bismuth chloride solution containing dimethyl sulfoxide, followed by a galvanic replacement process to deposit Bi clusters on surfaces of the substrate to generate the initial Bi layer. With the advancement of galvanic replacement reduction, the vertical bismuthene arrays were eventually formed with pronounced advantages, including high surface areas for fast charge transfer, affluent porosities for considerably reducing CO_2 molecule diffusion as well as lowering formate migration resistance, and ultrafast electron transportability derived from intimate contact with the conductive copper substrate. The vertical bismuthene arrays demonstrated $FE_{formate}$ above 90% between −0.75 and −0.95 V *vs.* RHE in 0.5 M $KHCO_3$ solution. In addition, various solvents were selected to observe the growth of the bismuthene arrays, such as ethanol, ethylene glycol, *N*-methyl-2-pyrrolidone and *N*,*N*-dimethylmethanamide, but only *N*,*N*-dimethylmethanamide as the solvent shows expected morphologies analogous to dimethyl sulfoxide. This study

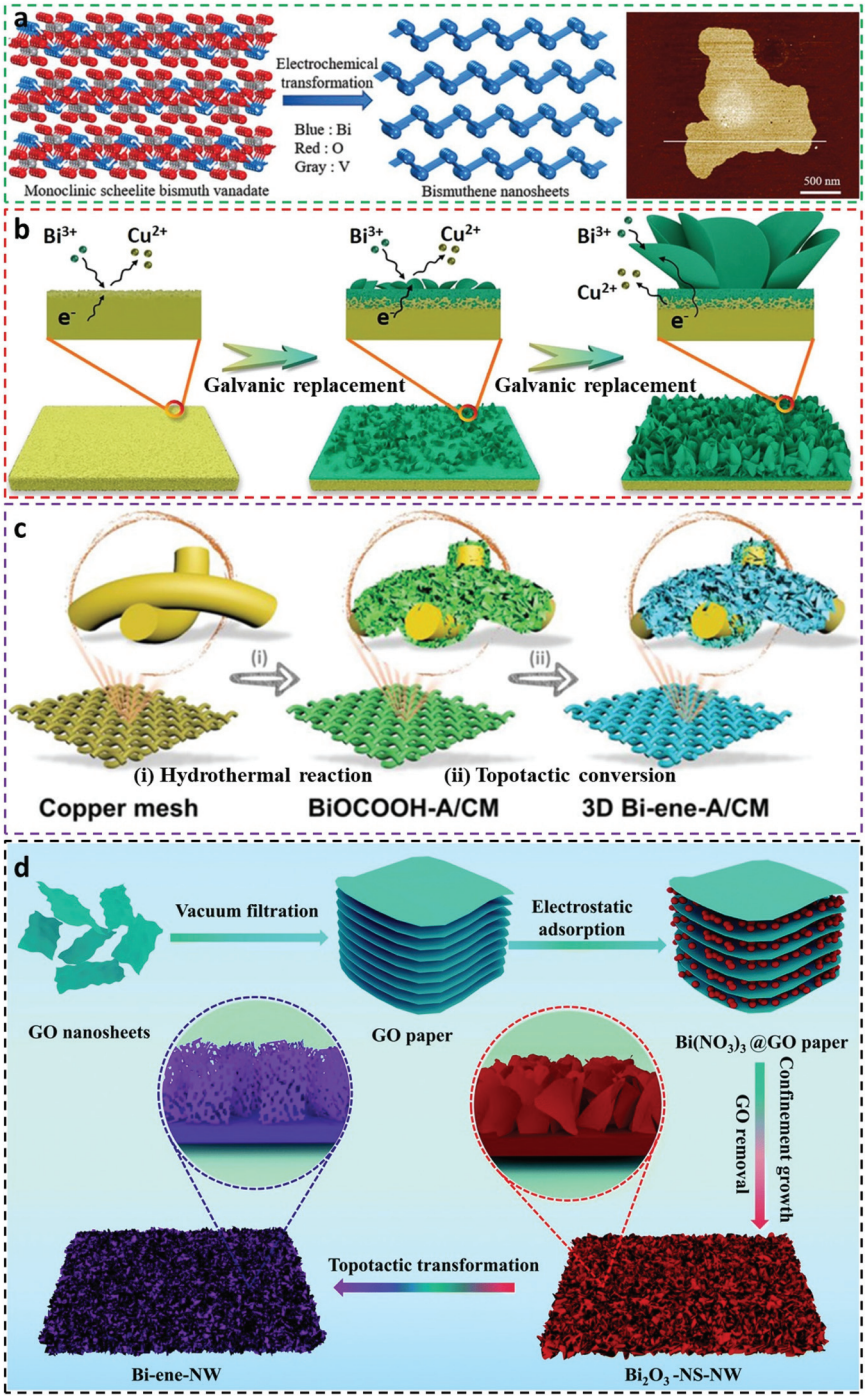

Fig. 4 Literature reported methods for the fabrication of bismuthene-related electrocatalysts for the CO_2RR. (a) Schematic descriptions of the synthesis of bismuthene nanosheets from monoclinic scheelite bismuth vanadate *via* the electrochemical transformation method, and AFM image of the bismuthene nanosheets.[7] This figure has been adapted from ref. 7 with permission from the John Wiley and Sons, copyright 2020. (b) Schematic illustration of growth of bismuthene nanosheets on Cu substrate *via* the galvanic replacement method.[36] This figure has been adapted from ref. 36 with permission from the John Wiley and Sons, copyright 2021. (c) Schematics of general process for the preparation of interconnected bismuthene arrays integrated with the 3D open network (Bi-ene-A/CM) *via* the topotactic conversion method.[47] This figure has been adapted from ref. 47 with permission from the John Wiley and Sons, copyright 2021. (d) Schematic demonstration of the fabrication of bismuthene (Bi-ene-NW) *via* the topotactic conversion method.[52] This figure has been adapted from ref. 52 with permission from the Royal Society of Chemistry.

offers an effective synthetic method to alter bismuthene electrocatalysts with novel morphologies, and can be expanded to other types of CO_2RR electrocatalysts.

To fabricate bismuthene electrocatalysts with an array morphology and industrial-level CO_2RR prospects (*e.g.* $FE_{formate}$ >90%, current density >200 mA cm^{-2}), He *et al.* employed a hydrothermal method to yield layered BiOCOOH arrays on the surface of copper mesh (CM), followed by an electrochemical topotactic conversion approach to prepare 3D interconnected bismuthene arrays with an open network (Bi-ene-A/CM, here Bi-ene and A stand for bismuthene and arrays, respectively).[47] The detailed preparation procedures are illustrated in Fig. 4c. As the superior advantages of array microstructures, the Bi-ene-A/CM delivered distinguished $FE_{formate}$ selectivity and current density in an H-type cell using 0.5 M $KHCO_3$ electrolyte, with the largest $FE_{formate}$ of 96.02% and a current density of 21.21 mA cm^{-2} at −0.88 V *vs.* RHE. At a current density of ~200 mA cm^{-2}, the exceptional and long-term stable CO_2RR performances of Bi-ene-A/CM were further embodied in both KCl and $KHCO_3$ electrolytes in a gas-diffusion flow cell, reaching a commercial $FE_{formate}$ selectivity of 92.57% and 93.65%, respectively. This methodology can be applied to construct ultrathin metallic electrocatalysts on different substrates that possess the potential for industrialization and commercialization. Another 3D-structured bismuthene electrocatalyst showing techno-economic interests was prepared by Zhang *et al. via* the innovative nanocarbon-mediated electrochemical topotactic conversion method (Fig. 4d).[52] In the study, a graphene oxide (GO) paper, with internal nanospaces formed by interlayer sheets, was utilized as a soft template for the uniform decoration of the $Bi(NO_3)_3$ species. Subsequent drying resulted in the shrinkage of the GO interlayer distance and also the even distribution of the bismuth salts on the GO surface. Thermal annealing in air led to the removal of GO paper by burning and in turn resulted in the formation of interconnected Bi_2O_3 network precursors. Finally, the bismuthene (Bi-ene-NW) electrocatalyst was acquired by the electrochemical topotactic conversion of the Bi_2O_3 precursors. This well-designed methodology therefore imparted the Bi-ene-NW with unique characteristics, such as ultrathin layers, large quantities of defects and rough plane edges, and open pores in the in-plane edges. Experimental CO_2RR results confirmed the ultrahigh catalytic activity of Bi-ene-NW in both the H-type cell and gas-diffusion flow cell scenarios. For the H-type cell, a peak $FE_{formate}$ selectivity of ~95% emerged at −0.9 V *vs.* RHE and also showed continuous operational ability for 500 h at a high current density of ~100 mA cm^{-2} without current decaying signs. Assays in a gas-diffusion flow cell revealed that the Bi-ene-NW electrocatalyst was able to work stably up to 100 h in 1 M $KHCO_3$ solution with a current density of ~200 mA cm^{-2}, meanwhile preserving undecayed $FE_{formate}$ (>90%), disclosing high commercial feasibility.

Despite numerous studies focusing on modulating the specified lattice planes, electrolytes, structures and morphologies of pure Bi electrocatalysts, reported methods for directly building 3D structures and efficiently introducing pores on the catalyst surface are scarce. Fortunately, the latest advanced methodologies pave the way for designing structurally sophisticated but innovative electrocatalysts for future studies. Examples encompass: (i) the electrochemical transformation of structure-dependent inorganic precursors; (ii) galvanic replacement reaction with attempts on multiple substrates or solvents; (iii) the integration of multiple synthetic steps; (IV) assistance by easily removable templates. Such 3D metallic electrocatalysts have the physicochemical advantages of exposing more accessible sites for enhancing catalytic performance, hierarchical microchannels for reducing mass transport resistances, and highly interconnected contacts for fast electron transfer, which lend them high electrocatalytic activities and stabilities. Consequently, 3D metallic electrocatalysts with a multitude of morphologies, thinner layers and defects (pores, lattice mismatch and strains, oxygen vacancies, *etc.*) are urgently needed to be developed, and an understanding of their structure–property correlation is required.

Bi nanosheet-related electrocatalysts

Beyond Bi nanoparticles and bismuthene electrocatalysts, Bi nanosheets also draw tremendous attention for the electroreduction of CO_2 to formate. One of the representative studies was reported by Han *et al.*,[65] where the ultrathin Bi nanosheets with exceptional formate selectivity ($FE_{foramte}$ of ~100% with a current density of 24 mA cm^{-2} at −1.7 V *vs.* RHE) were gained by the *in situ* topotactic transformation of bismuth oxyiodide (BiOI) nanosheets. Later, Liu *et al.* adopted a similar way to produce Bi nanosheets from BiOI, which showed a high $FE_{foramte}$ (95%) at a lower overpotential of −0.9 V *vs.* RHE, but the current density was only 13.3 mA cm^{-2}.[67] By using BiOBr nanosheets with an exposed (001) surface as precursors, Fu *et al.* successfully fabricated porous Bi nanosheets possessing the (001) surface with rich grain boundaries *via* topotactic transformation.[69] The porous Bi nanosheets showed a $FE_{foramte}$ of 95.2% at −1.4 V *vs.* RHE. DFT calculations explained that the excellent CO_2RR performance originated from the grain boundary-containing (001) surface endowing lower adsorption energy to the intermediate *OCHO. Most recently, Peng *et al.* initially made bismuth oxide with hydrangea-like shapes as a Bi nanosheet precursor, followed by converting it into ultrathin Bi nanosheets using topotactic transformation.[71] As expected, the ultrathin Bi nanosheets exhibited an outstanding $FE_{foramte}$ selectivity (~96%) in a broad range of overpotentials (from −0.78 V to −1.18 V *vs.* RHE). The above examples suggest that the precursor determines the finial morphology, fashion, geometry and physicochemical properties of Bi electrocatalysts, therefore attention should be paid to precursor synthesis, design, composition and selection in future studies.

Facile deposition of Bi nanosheets on a gas diffusion layer was developed by Wang *et al.*, which resulted in an excellent formate production ability of 91.5%.[73] Later, the catalyst leaching behaviors of Bi particle-deposited gas-diffusion electrodes in the CO_2RR were studied by Bienen *et al.*[74] Other Bi-relevant formats, such as Bi nanoflowers ($FE_{formate}$ of 99.2% at −1.5 V

vs. saturated calomel electrode),[75] microflowers ($FE_{formate}$ of ~96.2% at −0.80 to −1.50 V *vs.* RHE),[76] core–shell structures ($FE_{formate}$ of 99% at −1.0 V *vs.* RHE),[77] ultrathin Bi nanosheets (92.5% at −0.97 V *vs.* RHE),[3] Bi nanostructures ($FE_{formate}$ of 92% at −1.5 V *vs.* RHE),[78] Bi nanosheets with different sizes and thicknesses ($FE_{formate}$ of 92% at −0.9 V *vs.* RHE),[13] *etc.* have also been reported with promising electrocatalytic CO_2RR activities and capabilities. The remarkably high $FE_{formate}$ of 100% at an optimal overpotential of −0.86 V *vs.* RHE was achieved by using Bi nanoparticles/Bi_2O_3 nanosheets, which were accredited to the grain boundaries exposing considerably favorable active sites and stabilizing reaction intermediates.[16] Similarly, Bi/Bi_2O_3 junction nanosheets with defect-rich hierarchical mesopores were demonstrated by Wu *et al.*, which exhibited a $FE_{formate}$ of 90.4% at −0.87 V *vs.* RHE.[39]

All currently reported preeminent Bi electrocatalysts were only reported for formate production using liquid-state electrolytes, which require additional, energy-intensive and complex downstream separations to obtain the ready-to-collect formic acid products. To directly yield formic acid (HCOOH) products instead of formate, Xia *et al.* applied a CO_2RR reduction cell with a three-chamber configuration that utilized a solid-state electrolyte (SSE), anion exchange membrane (AEM) and cation exchange membrane (CEM) to achieve the objective.[42] The working principles of the three-chamber cell comprise four parts: the negatively charged species generated by the CO_2RR (*e.g.* $HCOO^-$, CH_3COO^-, *etc.*) will pass through the AEM driven by the electrical field; positively charged species (*i.e.* H^+) produced by either hydrogen oxidation reaction (HOR) or oxygen evolution reaction will traverse the CEM; the oppositely charged species will recombine in the middle SSE to compensate charges then forming high-quality pure liquid fuel solutions (*e.g.* HCOOH, CH_3COOH, *etc.*). This study further upgraded the already distinct three-chamber reduction cell to a four-chamber configuration for concurrently generating three valuable products of HCOOH, KOH and Cl_2. The Bi nanosheets in the typical H-type cell reached a $FE_{formate}$ of up to 99% at −0.79 V *vs.* RHE, and peaked at a FE of 93.1% for HCOOH at a cell voltage of 3.08 V in the three-chamber reduction cell. The capabilities of continuous working up to 100 h at 30 mA cm^{-2} and constant production of ~0.11 M pure HCOOH solution were also proved in this study. The broad applicability of this three-chamber configuration was further examined to produce pure C_{2+} carbonaceous products using Cu catalysts, including ethanol, *n*-propanol and acetic acid. A later example using the same strategy for the production of high-concentration pure formic acid (up to ~100 wt%) with significantly improved properties (*e.g.* current density, faradaic efficiency and operational stability) was reported by Fan *et al.*,[50] by using grain boundary-abundant Bi nanoparticles. These studies demonstrate the advantages of solid-state electrolytes in synthesizing high-quality and pure liquid fuels, with high potential to realize techno-economic prospects and commercialization.

The direct synthesis of ready-to-collect liquid products shows high practical significances and commercial values, hence, future efforts and trials shall also place on inventing sophisticated CO_2RR reduction cells to meet the requirements of property-differing and structurally complex reduction products, such as electrocatalytic CO_2 reduction to organonitrogen compounds.[79,80] On the other hand, the current density for the continuous production of HCOOH with long-time running showing no signs of decays was generally maintained at 30 mA cm^{-2} in the three-chamber reduction cell, indicative of more development spaces to enlarge it to a profitable level. As a result, the previously mentioned unary Bi-relevant electrocatalysts with prominent current density and long-term amperometric stability are worth examining for their HCOOH producibility in the three-chamber CO_2RR reduction cell, along with various promising CO_2 electrocatalysts for other value-added CO_2RR products.

Binary BiSn-based electrocatalysts

Sn is a well-known non-noble metal of low cost, environmental friendliness and with high supply reserves. However, the crucial point to construct BiSn bimetallic electrocatalysts for the CO_2RR is that Sn-based electrocatalysts share analogous electrocatalytic properties to Bi-based electrocatalysts. Both catalysts possess the leading abilities to efficiently and effectively produce formate/formic acid. Single-atom Sn electrocatalysts are excluded in the discussion because they may produce CO according to the Sn atomic configurations, due to different electrocatalytic reaction routes.[81–83] For example, Ni *et al.* designed Sn-based single-atom catalysts with a coordination configuration of Sn-C_2O_2F, which enabled the effective electrocatalytic conversion of CO_2 to CO with a FE value of up to 95.2%.[82] As a consequence, Sn tends to be integrated with Bi to form BiSn bimetallic electrocatalysts for the research community to comprehensively investigate CO_2RR-associated parameters, performances and product selectivity, but showing lower frequency compared with other types of binary metallic electrocatalysts.[84–88] Despite all this, recent discoveries with respect to BiSn binary electrocatalysts for the CO_2RR have been systematically reviewed in this section (Table 2).

Sn nanosheets as supports

A preliminary example was demonstrated by Wen *et al.*[10] They designed Bi–Sn bimetallic catalysts with favorable active sites formed by orbital interactions at the interfaces of the Bi nanoparticles and Sn nanosheets (Fig. 5a). In particular, the SnO nanosheets covered by a carbon fabric (CF) substrate precursor were synthesized by a hydrothermal reaction, followed by the introduction of Bi nanoparticles using electrodeposition at −0.1 V (*vs.* saturated calomel electrode) to form the CF-supported BiSn (BiSn/CF) electrocatalyst (Fig. 5b). The as-prepared BiSn/CF electrocatalyst exhibited much higher electrocatalytic activity than the un-deposited counterparts (Fig. 5c) and showed an optimal $FE_{formate}$ of 96% at −1.14 V *vs.* RHE (Fig. 5d). DFT calculations revealed that the deposition of Bi nanoparticles upshifted away Sn electron states from the

Table 2 Summary of binary BiSn-based electrocatalysts for the CO_2RR in aqueous electrolytes

Catalysts	Synthesis method	Morphology	Electrolyte	Cell	Products	Current density [mA cm^{-2}]	FE (%, *vs.* RHE)	Stability (h)	Ref.
BiSn bimetallic structures	Hydrothermal and electrodeposition method	Nanosheets supported nanoparticles	0.5 M $KHCO_3$	H-Type	Formate	—	96% at −1.14 V	—	10
Bi-Doped SnO nanosheets	Hydrothermal growth on Cu foam	Interconnected nanosheets	0.1 M $KHCO_3$	H-Type	Formate	~12	93% at −1.7 V *vs.* Ag/AgCl	30	14
Bi–Sn oxides	Hydrothermal synthesis	Nanoparticles supported by nanosheets	0.1 M $KHCO_3$	H-Type	Formate	~3.5	80% at −1.0 V	12 h at −1.0 V	24
Sn-Doped Bi_2O_3 nanosheets	Solvothermal method	Nanoparticles supported by nanosheets	0.5 M $KHCO_3$	H-Type	Formate	24.3	93.4% at −0.97 V	8	40
Eutectic BiSn nanoalloys	Liquid phase ultrasonication	Nanoparticles	0.1 M $KHCO_3$	H-Type	Formate	~8.5	78% at −1.1 V	—	2
BiSn alloys	Thermal evaporation	Bulk crystals	1 M $KHCO_3$ and KOH	Gas diffusion	Formate	100, 200, 300	~95.8%	2400 (100 mA cm^{-2}, at ~0.9 V)	18
Sn-Doped Bi/BiO_x core–shell nanowires	Electrochemical dealloying	Nanowires surrounded by core–shell nanoparticles	1.0 M KOH	Gas diffusion	Formate	~100	~100 at −0.7 V	20	1
Bi@Sn core–shells nanoparticles	Electrochemical conversion	Spherical nanoparticles	0.5 M $KHCO_3$	H-Type	Formate	~32	91% at −1.1 V	20 (at −0.9 V)	17
Bi@Sn core–shell nanoparticles	Electrochemical conversion	Spherical nanoparticles	2.0 M $KHCO_3$	Gas diffusion	Formate	200	~92% at −1.1 V	8	17
Bi-Doped amorphous SnO_x nanoshells	Wet-chemical reduction	Spherical nanoparticles	0.5 M $KHCO_3$	Gas diffusion	Formate	20.9	95.8% at −0.88 V	50	8
BiSn bimetallic structure	Two-step electrodeposition method	Velvet networks with pine needle-shaped dendrites	0.1 M $KHCO_3$	H-Type	Formate	34	94.8% at −1.0 V	20	61

Fermi level, resulting in a favorable adsorption energy on the Bi–Sn surface towards the *OOCH intermediates (Fig. 5e). Later, Cu foam as a growth substrate was applied to support Bi-doped SnO nanosheets by a hydrothermal reaction, which enabled to efficiently convert CO_2 to formate: a high $FE_{foramte}$ of 93% at −1.7 V (*vs.* Ag/AgCl) with a current density of 12 mA cm^{-2} and long-term stability of up to 30 h.[14] Two important aspects impacted the excellent electrocatalytic performance, namely Bi doping and electron transfer from the catalyst to Cu foam resisted the electroreduction of Sn^{2+} to Sn^0 during the CO_2RR, therefore giving rise to a lower energy barrier for the adsorption of HCOO* intermediates at the Bi SnO(001)/Cu surface. Doping is a facile and highly effective way to construct orbital hybridization between heterogeneous atoms to form altered electron states on different facets to reduce the adsorption energy towards electrocatalytic intermediates. Additionally, substrates as supports for electrocatalyst growth also play important roles in upholding electrocatalytic activities and maintaining their electronic states. Notably, both of the above cases adopted a binder-free approach to make electronic resistance-uncompromised electrodes, which can be extended in other electrocatalyst scenarios.

Bi nanosheets as supports

To inhibit the *in situ* reduction of SnO_2 during the CO_2RR process, Tian *et al.* fabricated SnO_2/Bi_2O_3 heterojunction oxides with strong interfacial interactions by using Bi_2O_3 sheets to distribute the SnO_2 nanoparticles. The interfacial interactions not only imparted SnO_2 nanoparticles with rich electrons but also protected the active site from being reduced. As a result, these Bi–Sn oxides showed $FE_{formate}$ values above 76% in a large overpotential window ranging from −1.0 to −1.4 V *vs.* RHE.[24] The $FE_{formate}$ selectivity was further greatly enhanced to 93.4% at −0.97 V *vs.* RHE by using the same components and strategy, as recently reported by Li *et al.*[40] In this case, Bi_2O_3 nanosheets were also used to dope with various loadings of SnO_2 nanoparticles (1.2, 2.5, and 3.8%), with the optimal loading of 2.5%. The Bi_2O_3 nanosheets can well maintain the Sn^{4+} species as active sites during electrocatalysis, as confirmed by X-ray photoelectron spectroscopy (XPS). DFT calculations indicated significantly lower adsorption energy towards the OCHO* intermediate in the Sn-doped Bi_2O_3 nanosheets, in line with the prominent yield of formate. The strategy of using oxide nanosheets as anti-reduction supports for metal oxides is a simple way to preserve catalytically active sites, therefore this strategy also can be implemented to decorate SnO nanoparticles or multivalent SnO_x nanoparticles with different oxidation state nanosheets as supporting frameworks to advance CO_2RR studies. Additionally, the deeper mechanism of synergistic effects between metal oxides in future studies is worth investigating.

BiSn alloy electrocatalysts

Different formats of BiSn alloy electrocatalysts prepared by various means have also been developed to understand their electrocatalytic nature. For instance, Tang *et al.* synthesized

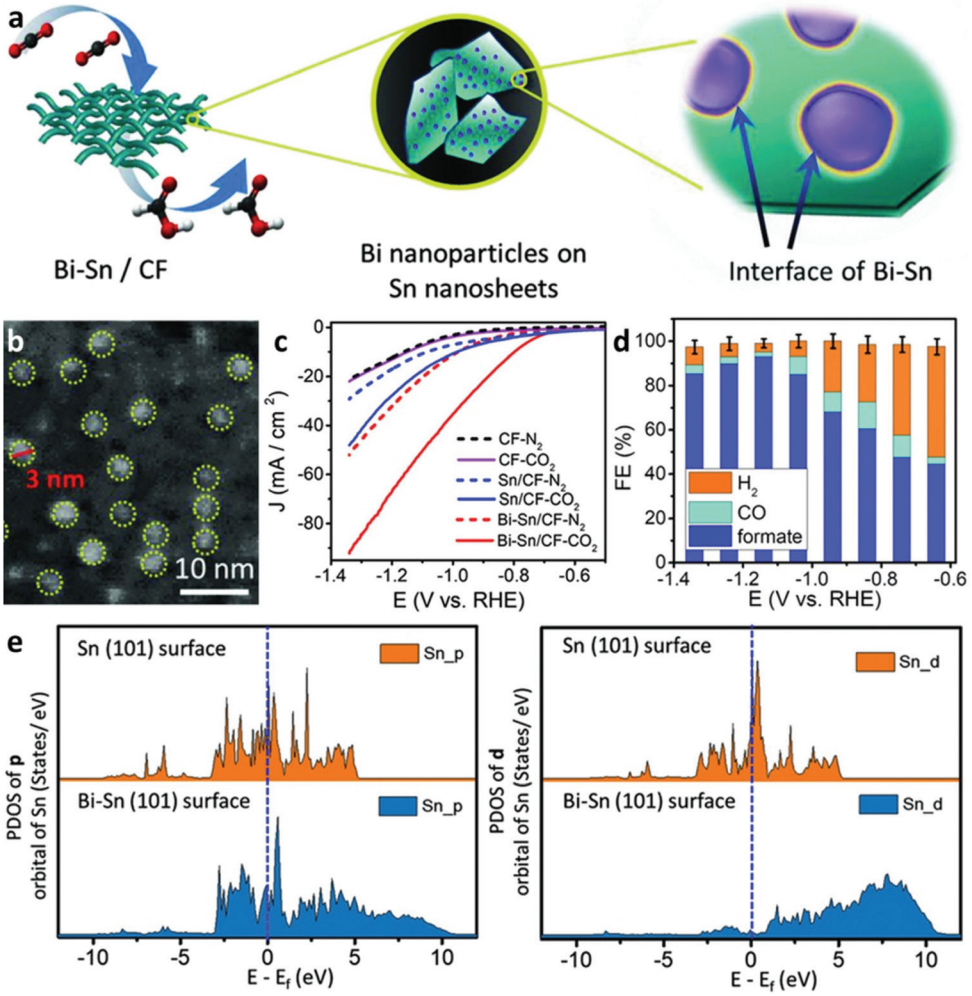

Fig. 5 (a) Schematic illustration of the synthesis for the Bi–Sn catalyst on carbon fabric (CF) substrate and demonstration of Bi nanoparticles anchored on the surface Sn nanosheets. (b) TEM image of the Bi–Sn catalyst. (c) Electrocatalytic activities of the Bi–Sn/CF, Sn/CF, and CF in a N_2- and CO_2-saturated 0.5 M $KHCO_3$ electrolyte. (d) Faradic efficiencies of generated products from the Bi–Sn catalyst at various potentials. (e) PDOS results of different orbitals of Sn atom on Sn (101) and Bi-Sn (101) surfaces before HCOO* adsorption.[10] This figure has been adapted from ref. 10 with permission from the John Wiley and Sons, copyright 2018.

eutectic BiSn alloy bulks by liquefying Bi and Sn metals, followed by liquid-phase ultrasonication at elevated temperature to re-configure and disperse the BiSn bulks into uniform nano-alloying nanoparticles, as shown in Fig. 6a.[2] As observed in Fig. 6b, the representative nanoalloys display elemental uniformities of Bi and Sn, with the oxidation-induced well distribution of O. The BiSn nanoalloys attained a peak value of $FE_{formate}$ of 78% at −1.1 V *vs.* RHE, outperforming non-eutectic counterparts, indicative of the advantages of eutectic alloys. The grain sizes and edge dislocations shaped in ratio-varied BiSn nanoalloys were visualized and discussed, providing a guideline for other binary eutectic alloy systems. This case sets a good example for future synthesis of more complex eutectic alloys, and the aid of liquid-phase ultrasonication shows the prospects of readily scaling up the production of eutectic nanoalloys.

An ultralong CO_2RR operation of up to 100 days with a stable current density of 100 mA cm^{-2} and $FE_{formate}$ >95% was measured over the alloyed $Bi_{0.1}Sn$ crystals (Fig. 6d), which were prepared by thermally evaporating BiSn precatalysts onto polytetrafluoroethylene (PTFE) substrates under an ultralow pressure (Fig. 6c).[18] This performance-exceptional ($FE_{formate}$ of 95.8% at an unprecedented partial current density of 74.6 mA cm^{-2}) $Bi_{0.1}Sn$ crystalline alloy was validated by STEM-EDS mapping, as observed in Fig. 6e. The ultralong electrocatalytic and structural stabilities of $Bi_{0.1}Sn$ alloy crystals were ascribed to the formed highly active $BiSn:SnO_2$ surfaces that enabled executing Sn/Sn^{4+} redox to protect active surfaces, while the superior catalytic activity towards the production of formate was attributed to the opportune binding energy to the *OCHO intermediate. The generation of concentrated formate solution up to 3.4 molar over 100 h in a membrane electrode assembly system was further demonstrated on the alloy crystals. In general, as exemplified by the above study, thermal evaporation can be a feasible approach for constructing structurally stable while catalytically distinguished alloy catalysts. New

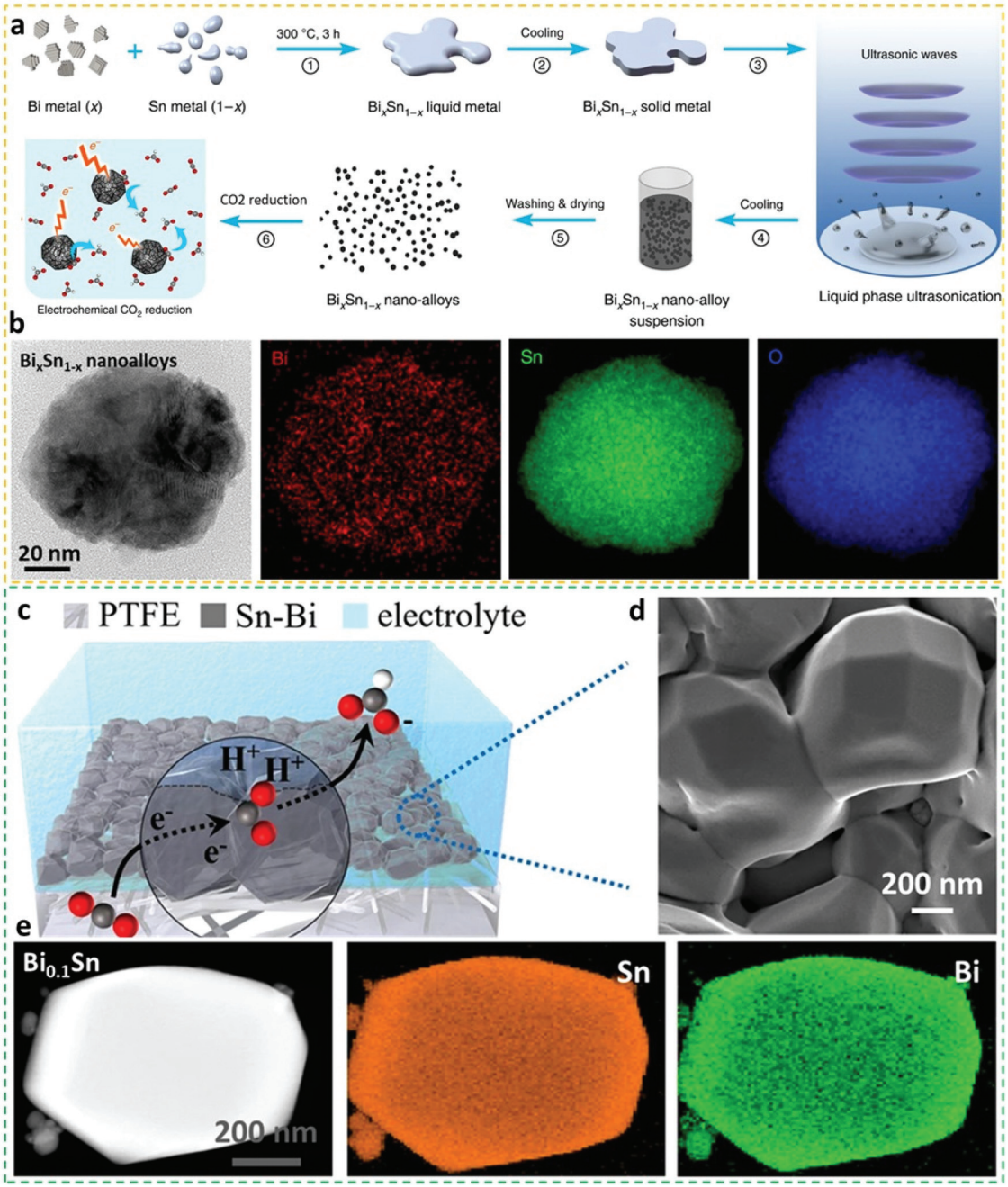

Fig. 6 (a) Schematics of the experimental steps to fabricate Bi_xSn_{1-x} nanoalloy electrocatalysts for CO_2RR applications. (b) STEM-EDX mapping images of the Bi_xSn_{1-x} nanoalloy electrocatalysts.[2] This figure has been adapted from ref. 2 with permission from the Springer Nature, copyright 2019. (c) Schematic illustration of $Bi_{0.1}Sn$ alloying electrocatalysts on a polytetrafluoroethylene (PTFE) gas diffusion layer. (d) SEM image of $Bi_{0.1}Sn$ alloying electrocatalysts. (e) STEM-EDS mapping images of the $Bi_{0.1}Sn$ alloying electrocatalyst.[18] This figure has been adapted from ref. 18 with permission from the Springer Nature, copyright 2021.

CO_2RR electrocatalysts can be synthesized by using different substrates (*e.g.* nanocarbons, films, foams or aerogels) or introducing new metallic entities or regimes *via* this method. The optimal amount of Bi in $Bi_{0.1}Sn$ alloys is relatively low, which is also a good sign for the incorporation of pricy and rare noble metals *via* the thermal evaporation method with the aid of more advanced tools.

BiSn core–shell electrocatalysts

Core–shell structures have shown promise in the field of electrocatalysis, due to their high surface areas, unique lattice effects, effective charge transportabilities, well-tailored electronic structures, and excellent structural stabilities.[89–92] Despite the synthesis of an Bi-relevant core–shell electrocata-

lyst for CO_2RR applications being less-frequently reported,[93] BiSn core–shell electrocatalysts have recently drawn immense attention and also have been prepared with different geometries and morphologies to investigate their electrocatalytic CO_2RR behaviors.

One-dimensional Bi/Bi(Sn)O_x core–shell nanowires (NWs) were constructed by electrochemically dealloying the Bi_1Sn_{99} alloy precursors (Fig. 7a).[1] The as-prepared Bi/Bi(Sn)O_x NWs showed diameters of around 10 nm and geometries of a highly conductive metallic Bi core surrounded by an Sn-doped BiO_x shell, as observed in the STEM image and the corresponding EDS mappings (Fig. 7b). As a consequence, the Bi/Bi(Sn)O_x NWs exhibited marked $FE_{formate}$ values (above 92%) over wide overpotential ranges (from −0.5 V to −0.9 V *vs.* RHE), attained an impressive current density (301.4 mA cm^{-2} at −1.0 V *vs.* RHE), and maintained distinct structural stability (up to 20 h at −0.7 V *vs.* RHE) in a gas diffusion flow cell. The superior catalytic activity was accredited to the introduction of Sn atoms into BiO_x species in the shell microstructures which benefits the stabilization of the *OCHO intermediate. A different strategy to synthesize the BiSn core–shell electrocatalyst for the CO_2RR was conducted by Xing *et al.*[17] In particular, the *in situ* electroreduction of $Bi_2Sn_2O_7$ nanoparticles was conducted to acquire the Bi@Sn core–shell nanoparticulate elec-

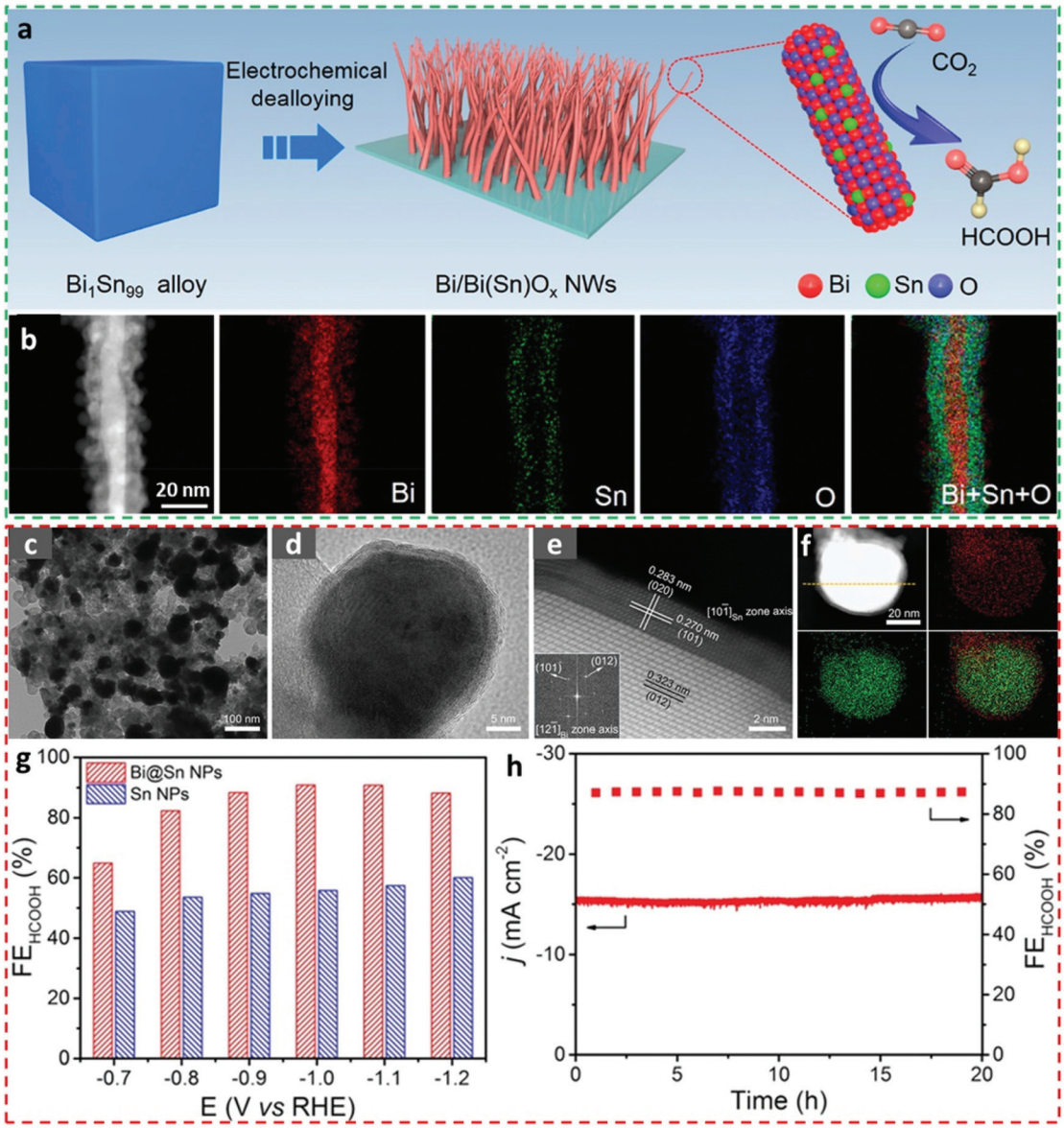

Fig. 7 (a) Schematic demonstration for synthesizing the Bi/Bi(Sn)O_x nanowires. (b) STEM-EDS mapping images of Bi/Bi(Sn)O_x nanowires.[1] This figure has been adapted from ref. 1 with permission from the American Chemical Society, copyright 2021. (c) TEM, (d) HRTEM, (e) HAADF-STEM images and (f) HAADF-STEM-EDX elemental mapping of the Bi@Sn nanoparticles. (g) The electrocatalytic products and (h) the potentiostatic measurements on the Bi@Sn nanoparticles.[17] This figure has been adapted from ref. 17 with permission from the John Wiley and Sons, copyright 2017.

trocatalysts (Fig. 7c and d), which consisted of a metallic Bi core and a layered Sn shell (Fig. 7e). Direct visual observation of the Bi@Sn core–shell microstructures was realized by HAADF-STEM-EDX elemental mapping, as shown in Fig. 7f. This Bi@Sn core–shell structure exhibited much higher catalytic formate production capability than that of direct chemical-reduction-obtained Sn nanoparticles owing to the compressive strain in the Sn shell (Fig. 7g), as exemplified by a remarkable $FE_{foramte}$ value of 91% at −1.1 V *vs.* RHE and a stable performance lasting for 20 h at −0.9 V *vs.* RHE in a H-type cell (Fig. 7h). Surprisingly, this Bi@Sn core–shell structure also presented high techno-economic possibility and suitability, as they can stably work at a current density of 200 mA cm^{-2} with almost no decaying signs while maintaining the $FE_{formate}$ of 92% in a gas flow-cell equipment using 2.0 M $KHCO_3$ as the electrolyte. This study shows a facile way to fabricate electrocatalysts with strong lattice stains, and therefore, the rational design of other core–shell systems can be encouraged by using this strategy and the wise selection of metal oxide precursors is of great importance.

Showing the advantages of both the above-mentioned one-dimensional Bi/Bi(Sn)O_x core–shell nanowires and performance-marked Bi@Sn core–shell nanoparticles, $Sn_{0.80}Bi_{0.20}$@Bi-SnO_x core–shell nanoparticles with the features of spherical morphologies (*i.e.* showing similar shapes and geometries with Bi@Sn nanoparticles) and exclusive Bi-doped amorphous SnO_x nanoshells (*i.e.* Sn-doped BiO_x shells in Bi/Bi(Sn)O_x nanowires) were fabricated by Yang *et al.*, as demonstrated in Fig. 8a and b.[8] The as-synthesized $Sn_{0.80}Bi_{0.20}$@Bi-SnO_x nanoparticles had average diameters of ~20 nm (Fig. 8b) and nanoshell thickness of 3.1 nm (Fig. 8c). The thick, well-alloyed, Bi-doped amorphous SnO_x nanoshells were visualized by the STEM-EDS technique, as seen in elemental mapping images in Fig. 8d–g. Owing to the unique geometries and easy flow of electrons from Bi to Sn, the $Sn_{0.80}Bi_{0.20}$@Bi-SnO_x nanoparticles showed prominent $FE_{formate}$ selectivities above 91.5% between −0.67 and −0.92 V *vs.* RHE in a gas-flow cell. The optimal $FE_{formate}$ value of 95.8% with a current density of 20.9 mA cm^{-2} emerged at −0.88 V *vs.* RHE. In terms of commercial interest, the current density, in this case, is relatively low, and potentiostatic working stability should also be assessed, meaning that additional structural optimization, heteroatom doping or introduction of other metal species for performance enhancements is applicable.

The recently reported various BiSn alloy electrocatalysts exhibit desirable selectivity towards formate production in both H-type and gas-flow cells, while none of them reached a commercial-level current density of 200 mA cm^{-2} and or being continuously operated to 100 h, consequently, future strategies or tactics can be developed on such excellent BiSn alloy electrocatalysts to accomplish the goals. Beyond these reported BiSn alloy electrocatalysts, other types of alloyed electrocatalysts and even high-entropy alloys are worth exploitation for addressing present CO_2RR challenges.

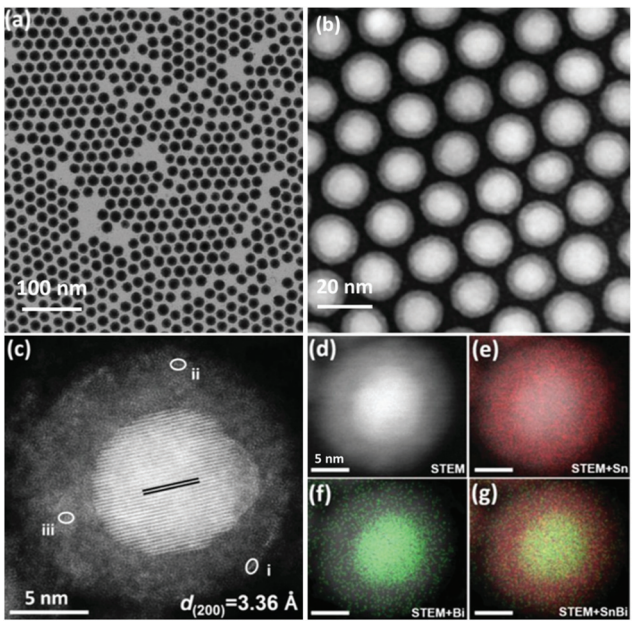

Fig. 8 (a) TEM, (b) HAADF-STEM, and (c) aberration-corrected HAADF-STEM images of the $Sn_{0.80}Bi_{0.20}$@Bi-SnO_x core–shell alloy nanoparticles. (d–g) STEM-EDS elemental mapping images of $Sn_{0.80}Bi_{0.20}$@Bi-SnO_x core–shell alloy nanoparticles.[8] This figure has been adapted from ref. 8 with permission from the John Wiley and Sons, copyright 2020.

Other BiSn hybrid electrocatalysts

With respect to Bi and S co-doped SnO_2 electrocatalysts for the CO_2RR, Li *et al.* utilized a one-step hydrothermal method.[94] Different doping ratios were investigated (0%, 1%, 3%, 5% and 7%), and the $FE_{formate}$ results indicated that 3% doping was the best enabling a $FE_{formate}$ of 55.6% at −1.0 V *vs.* Ag/AgCl. Noticeably, this (Bi, S) co-doped SnO_2 was also capable of functioning as an effective photocatalyst, signifying that the development and design of catalysts with bifunctionalities (*i.e.* electrocatalytic and photocatalytic) in future studies are in demand. Electrodeposition of composition-varied binary BiSn particles onto copper sheets as binder-free cathodic electrodes for CO_2RR measurements was attempted by Li *et al.*, and results substantiated that the FE_{foamte} value showed a positive correlation with the increment of Bi mole contents.[95] A recent study also adopted the electrodeposition method to deposit binary Bi_5Sn_{20}, Bi_5Sn_{40}, Bi_5Sn_{60} and Bi_5Sn_{80} onto copper meshes instead of copper sheets as binder-free cathodic electrodes, which gave rise to the formation of a pine needle-shaped dendritic morphology.[61] Among the as-prepared electrocatalysts, the Bi_5Sn_{60} yielded an enticing $FE_{formate}$ of up to 94.8%, promising working durability of up to 20 h and a slightly reduced current density of around 36 mA cm^{-2} at −1.0 V *vs.* RHE, owing to the pine needle-shaped dendrites offering myriad active sites and showing excellent stability.

As discussed above, simply alternating substrates while using the same preparation strategies will result in tremendously differentiated morphologies, which in turn greatly affects the final CO_2RR performance matrix, including product

selectivity, electrocatalytic activity, structural stability, and functionality under harsh conditions. One reason for the impressive FE of the Bi_5Sn_{60} electrocatalyst stems from its binder-free character, leading to well-preserved electron transfer efficiencies. Consequently, designing binder-free electrocatalysts for comprehensively elevating the CO_2RR performances is urgently needed and should be paid enormous attention in future investigations.

Conclusions and future outlook

The electrocatalytic CO_2RR is one of the environmental-friendly and efficient ways to mitigate CO_2-associated concerns while concurrently yielding value-added and profitable chemicals, especially formic acid that possesses the highest net present value. In this minireview, direct CO_2RR for the production of formate/formic acid over various recently published unary Bi-relevant electrocatalysts and binary BiSn-based electrocatalysts is comprehensively and systematically summarized, with an in-depth focus on their fabrication methodologies, material morphologies, catalytic performances and mechanisms. For the unary Bi electrocatalysts, recent advances on different nanoparticles, bismuthene and nanosheets were classified and their corresponding electrocatalytic functionalities were elucidated. Exposing crystalline facets and modulating morphologies play crucial roles in determining the catalytic activity affecting the final FE towards formate. Additionally, the direct electrocatalytic CO_2RR to ready-to-collect formic acid was validated by using solid state electrolytes in four-chamber cell configurations, disclosing techno-economic prospects and high likelihood of commercialization, also underlining the significant importance of employing solid state electrolytes in future CO_2RR studies. Reported binary BiSn electrocatalysts with similar morphologies are carefully categorized, mainly focusing on electrocatalysts with different formats, alloying and core–shell structures. Essentially, catalytic performances (FE, stability and durability, *etc.*) from similar electrocatalysts were compared and insights into mechanisms were elucidated.

To further enhance electrocatalytic CO_2RR performances over Bi-based electrocatalysts, several perspectives are proposed. Despite Bi-based electrocatalysts having shown remarkable selectivity and faradaic efficiency towards the production of formic acid, most of them face a low current density dilemma. Reducing the particle size, creating structure-stable defects, introducing heteroatoms, forming alloy microstructures and exposing exclusive facets are essential to boost electrocatalytic activity, in turn improving current density during the CO_2RR. Explorations regarding Bi single-atom and dual-atom electrocatalysts are scarcely reported, while singe-atom and dual-atom electrocatalysts have been revealed displaying unprecedented electrocatalytic CO_2RR capacities and performances, as a result, those should be urgently fabricated and explored to comprehend their electrocatalytic behaviors and products. In terms of electrochemical transformation, the morphology and known exposed facets of catalyst precursors are key to attain performance-enhanced electrocatalysts, as a consequence, the wise selection and purposed synthesis of catalyst precursors are excellent strategies. Additionally, binder-free catalysts display outstanding electrocatalytic activities and high faradaic efficiencies of customized products, hence, tactics to deposit electrocatalysts onto different substrates should be developed, for which the thermal shock method is highly available and feasible. Nanocarbon materials have shown high prospects as substrates to form binder-free electrocatalysts, which is worth further exploration. Furthermore, high entropy alloys present remarkable functionalities in the areas of electrocatalysis, while Bi-relevant high entropy alloys have not been demonstrated in CO_2RR considerations. For directly obtaining high-purity and concentrated CO_2RR products, solid state electrolytes are of great significance. The current conundrums concerning reaching up to commercial current density with long-term operationability must be addressed, for which, already reported distinct electrocatalysts should be employed in solid state electrolyte systems. It is hoped that more CO_2RR applications using Bi-related electrocatalysts will be considerably expedited in the near future.

Conflicts of interest

There are no conflicts to declare.

Acknowledgements

This work was supported by the National Natural Science Foundation of China (grant no. 21703248), and the National Key Research and Development Program of China (grant no. 2017YFA0700103, 2018YFA0704502). Magdalena Titirici would like to thank to the RAEng CiET1819\2\60.

Notes and references

1 Y. Zhao, X. Liu, Z. Liu, X. Lin, J. Lan, Y. Zhang, Y.-R. Lu, M. Peng, T.-S. Chan and Y. Tan, *Nano Lett.*, 2021, **21**, 6907–6913.
2 J. Tang, R. Daiyan, M. B. Ghasemian, S. A. Idrus-Saidi, A. Zavabeti, T. Daeneke, J. Yang, P. Koshy, S. Cheong, R. D. Tilley, R. B. Kaner, R. Amal and K. Kalantar-Zadeh, *Nat. Commun.*, 2019, **10**, 4645.
3 D. Wu, X. Shen, J. Liu, C. Wang, Y. Liang, X.-Z. Fu and J.-L. Luo, *Nanoscale*, 2019, **11**, 22125–22133.
4 S. Nitopi, E. Bertheussen, S. B. Scott, X. Liu, A. K. Engstfeld, S. Horch, B. Seger, I. E. L. Stephens, K. Chan, C. Hahn, J. K. Nørskov, T. F. Jaramillo and I. Chorkendorff, *Chem. Rev.*, 2019, **119**, 7610–7672.
5 Y. Li, B. Wei, M. Zhu, J. Chen, Q. Jiang, B. Yang, Y. Hou, L. Lei, Z. Li, R. Zhang and Y. Lu, *Adv. Mater.*, 2021, **33**, 2102212.

6 F. Yang, X. Ma, W.-B. Cai, P. Song and W. Xu, *J. Am. Chem. Soc.*, 2019, **141**, 20451–20459.
7 W. Ma, J. Bu, Z. Liu, C. Yan, Y. Yao, N. Chang, H. Zhang, T. Wang and J. Zhang, *Adv. Funct. Mater.*, 2021, **31**, 2006704.
8 Q. Yang, Q. Wu, Y. Liu, S. Luo, X. Wu, X. Zhao, H. Zou, B. Long, W. Chen, Y. Liao, L. Li, P. K. Shen, L. Duan and Z. Quan, *Adv. Mater.*, 2020, **32**, 2002822.
9 F. Yang, A. O. Elnabawy, R. Schimmenti, P. Song, J. Wang, Z. Peng, S. Yao, R. Deng, S. Song, Y. Lin, M. Mavrikakis and W. Xu, *Nat. Commun.*, 2020, **11**, 1088.
10 G. Wen, D. U. Lee, B. Ren, F. M. Hassan, G. Jiang, Z. P. Cano, J. Gostick, E. Croiset, Z. Bai, L. Yang and Z. Chen, *Adv. Energy Mater.*, 2018, **8**, 1802427.
11 H. Xie, T. Zhang, R. Xie, Z. Hou, X. Ji, Y. Pang, S. Chen, M.-M. Titirici, H. Weng and G. Chai, *Adv. Mater.*, 2021, **33**, 2008373.
12 S. M. Jordaan and C. Wang, *Nat. Catal.*, 2021, **4**, 915–920.
13 P. Liu, H. Liu, S. Zhang, J. Wang and C. Wang, *J. CO2 Util.*, 2021, **51**, 101643.
14 X. An, S. Li, A. Yoshida, T. Yu, Z. Wang, X. Hao, A. Abudula and G. Guan, *ACS Appl. Mater. Interfaces*, 2019, **11**, 42114–42122.
15 X. Chen and B. Lin, *Energy Policy*, 2021, **157**, 112510.
16 L. Li, D.-K. Ma, F. Qi, W. Chen and S. Huang, *Electrochim. Acta*, 2019, **298**, 580–586.
17 Y. Xing, X. Kong, X. Guo, Y. Liu, Q. Li, Y. Zhang, Y. Sheng, X. Yang, Z. Geng and J. Zeng, *Adv. Sci.*, 2020, **7**, 1902989.
18 L. Li, A. Ozden, S. Guo, F. P. García de Arquer, C. Wang, M. Zhang, J. Zhang, H. Jiang, W. Wang, H. Dong, D. Sinton, E. H. Sargent and M. Zhong, *Nat. Commun.*, 2021, **12**, 5223.
19 R. Zhao, P. Ding, P. Wei, L. Zhang, Q. Liu, Y. Luo, T. Li, S. Lu, X. Shi, S. Gao, A. M. Asiri, Z. Wang and X. Sun, *Adv. Funct. Mater.*, 2021, **31**, 2009449.
20 W. Lai, Z. Ma, J. Zhang, Y. Yuan, Y. Qiao and H. Huang, *Adv. Funct. Mater.*, 2022, 2111193.
21 J. Yu, J. Wang, Y. Ma, J. Zhou, Y. Wang, P. Lu, J. Yin, R. Ye, Z. Zhu and Z. Fan, *Adv. Funct. Mater.*, 2021, **31**, 2102151.
22 Y. Zheng, P. Cheng, J. Xu, J. Han, D. Wang, C. Hao, H. R. Alanagh, C. Long, X. Shi and Z. Tang, *Nanoscale*, 2019, **11**, 4911–4917.
23 J. Jiao, R. Lin, S. Liu, W.-C. Cheong, C. Zhang, Z. Chen, Y. Pan, J. Tang, K. Wu, S.-F. Hung, H. M. Chen, L. Zheng, Q. Lu, X. Yang, B. Xu, H. Xiao, J. Li, D. Wang, Q. Peng, C. Chen and Y. Li, *Nat. Chem.*, 2019, **11**, 222–228.
24 J. Tian, R. Wang, M. Shen, X. Ma, H. Yao, Z. Hua and L. Zhang, *ChemSusChem*, 2021, **14**, 2247–2254.
25 Y. Cai, J. Fu, Y. Zhou, Y.-C. Chang, Q. Min, J.-J. Zhu, Y. Lin and W. Zhu, *Nat. Commun.*, 2021, **12**, 586.
26 T. Zhang, W. Li, K. Huang, H. Guo, Z. Li, Y. Fang, R. M. Yadav, V. Shanov, P. M. Ajayan, L. Wang, C. Lian and J. Wu, *Nat. Commun.*, 2021, **12**, 5265.
27 X.-C. Liu, C. Wei, Y. Wu, Y. Fang, W.-Q. Li, R.-R. Ding, G. Wang and Y. Mu, *ACS Catal.*, 2021, **11**, 14986–14994.
28 Z. Zhang, F. Ahmad, W. Zhao, W. Yan, W. Zhang, H. Huang, C. Ma and J. Zeng, *Nano Lett.*, 2019, **19**, 4029–4034.
29 Q. Zhao, C. Zhang, R. Hu, Z. Du, J. Gu, Y. Cui, X. Chen, W. Xu, Z. Cheng, S. Li, B. Li, Y. Liu, W. Chen, C. Liu, J. Shang, L. Song and S. Yang, *ACS Nano*, 2021, **15**, 4927–4936.
30 R. Francke, B. Schille and M. Roemelt, *Chem. Rev.*, 2018, **118**, 4631–4701.
31 Z. Yin, C. Yu, Z. Zhao, X. Guo, M. Shen, N. Li, M. Muzzio, J. Li, H. Liu, H. Lin, J. Yin, G. Lu, D. Su and S. Sun, *Nano Lett.*, 2019, **19**, 8658–8663.
32 J. Yin, Z. Gao, F. Wei, C. Liu, J. Gong, J. Li, W. Li, L. Xiao, G. Wang, J. Lu and L. Zhuang, *ACS Catal.*, 2022, 1004–1011, DOI: **10.1021/acscatal.1c04714**.
33 P. Lu, D. Gao, H. He, Q. Wang, Z. Liu, S. Dipazir, M. Yuan, W. Zu and G. Zhang, *Nanoscale*, 2019, **11**, 7805–7812.
34 D. Gao, I. Zegkinoglou, N. J. Divins, F. Scholten, I. Sinev, P. Grosse and B. R. Cuenya, *ACS Nano*, 2017, **11**, 4825–4831.
35 W. Ma, S. Xie, T. Liu, Q. Fan, J. Ye, F. Sun, Z. Jiang, Q. Zhang, J. Cheng and Y. Wang, *Nat. Catal.*, 2020, **3**, 478–487.
36 J. Fan, X. Zhao, X. Mao, J. Xu, N. Han, H. Yang, B. Pan, Y. Li, L. Wang and Y. Li, *Adv. Mater.*, 2021, **33**, 2100910.
37 L. Fan, C. Xia, F. Yang, J. Wang, H. Wang and Y. Lu, *Sci. Adv.*, 2020, **6**, eaay3111.
38 H. Guzmán, N. Russo and S. Hernández, *Green Chem.*, 2021, **23**, 1896–1920.
39 D. Wu, G. Huo, W. Chen, X.-Z. Fu and J.-L. Luo, *Appl. Catal., B*, 2020, **271**, 118957.
40 X. Li, X. Wu, J. Li, J. Huang, L. Ji, Z. Leng, N. Qian, D. Yang and H. Zhang, *Nanoscale*, 2021, **13**, 19610–19616.
41 X. Wei, W. Zhang, D. Liu, D. Liu, Y. Yan, J. Zhang, Y. Yang, S. Yan and Z. Zou, *J. CO2 Util.*, 2022, **55**, 101797.
42 C. Xia, P. Zhu, Q. Jiang, Y. Pan, W. Liang, E. Stavitski, H. N. Alshareef and H. Wang, *Nat. Energy*, 2019, **4**, 776–785.
43 M. Jouny, W. Luc and F. Jiao, *Ind. Eng. Chem. Res.*, 2018, **57**, 2165–2177.
44 Y. Minami and Y. Amao, *Sustainable Energy Fuels*, 2020, **4**, 3458–3466.
45 P. Senthilkumar, M. Mohapatra and S. Basu, *RSC Adv.*, 2022, **12**, 1287–1309.
46 A. Klinkova, P. De Luna, C.-T. Dinh, O. Voznyy, E. M. Larin, E. Kumacheva and E. H. Sargent, *ACS Catal.*, 2016, **6**, 8115–8120.
47 Y.-C. He, D.-D. Ma, S.-H. Zhou, M. Zhang, J.-J. Tian and Q.-L. Zhu, *Small*, 2022, **18**, 2105246.
48 X. Zhang, T. Lei, Y. Liu and J. Qiao, *Appl. Catal., B*, 2017, **218**, 46–50.
49 A. Vasileff, C. Xu, L. Ge, Y. Zheng and S.-Z. Qiao, *Chem. Commun.*, 2018, **54**, 13965–13968.
50 L. Fan, C. Xia, P. Zhu, Y. Lu and H. Wang, *Nat. Commun.*, 2020, **11**, 3633.

51 W. Luo, W. Xie, M. Li, J. Zhang and A. Züttel, *J. Mater. Chem. A*, 2019, **7**, 4505–4515.
52 M. Zhang, W. Wei, S. Zhou, D.-D. Ma, A. Cao, X.-T. Wu and Q.-L. Zhu, *Energy Environ. Sci.*, 2021, **14**, 4998–5008.
53 F. Franco, C. Rettenmaier, H. S. Jeon and B. R. Cuenya, *Chem. Soc. Rev.*, 2020, **49**, 6884–6946.
54 W. Yu, L. Wen, J. Gao, S. Chen, Z. He, D. Wang, Y. Shen and S. Song, *Chem. Commun.*, 2021, **57**, 7418–7421.
55 T. E. Teeter and P. Van Rysselberghe, *J. Chem. Phys.*, 1954, **22**, 759–760.
56 Z.-Z. Wu, F.-Y. Gao and M.-R. Gao, *Energy Environ. Sci.*, 2021, **14**, 1121–1139.
57 L. Xie, J. Liang, C. Priest, T. Wang, D. Ding, G. Wu and Q. Li, *Chem. Commun.*, 2021, **57**, 1839–1854.
58 H. Jiang, L. Wang, Y. Li, B. Gao, Y. Guo, C. Yan, M. Zhuo, H. Wang and S. Zhao, *Appl. Surf. Sci.*, 2021, **541**, 148577.
59 Y. Guan, M. Liu, X. Rao, Y. Liu and J. Zhang, *J. Mater. Chem. A*, 2021, **9**, 13770–13803.
60 J. Gu, F. Héroguel, J. Luterbacher and X. Hu, *Angew. Chem., Int. Ed.*, 2018, **57**, 2943–2947.
61 Z. Li, Y. Feng, Y. Li, X. Chen, N. Li, W. He and J. Liu, *Chem. Eng. J.*, 2022, **428**, 130901.
62 S. Zhao, S. Li, T. Guo, S. Zhang, J. Wang, Y. Wu and Y. Chen, *Nano-Micro Lett.*, 2019, **11**, 62.
63 H. Rabiee, L. Ge, X. Zhang, S. Hu, M. Li and Z. Yuan, *Energy Environ. Sci.*, 2021, **14**, 1959–2008.
64 Y. J. Sa, C. W. Lee, S. Y. Lee, J. Na, U. Lee and Y. J. Hwang, *Chem. Soc. Rev.*, 2020, **49**, 6632–6665.
65 N. Han, Y. Wang, H. Yang, J. Deng, J. Wu, Y. Li and Y. Li, *Nat. Commun.*, 2018, **9**, 1320.
66 X. An, S. Li, X. Hao, Z. Xie, X. Du, Z. Wang, X. Hao, A. Abudula and G. Guan, *Renewable Sustainable Energy Rev.*, 2021, **143**, S1364032121002446.
67 P. Liu, H. Liu, S. Zhang, J. Wang and C. Wang, *J. Colloid Interface Sci.*, 2021, **602**, 740–747.
68 X. Lu, D. Y. C. Leung, H. Wang, M. K. H. Leung and J. Xuan, *ChemElectroChem*, 2014, **1**, 836–849.
69 X. Fu, J.-a. Wang, X. Hu, K. He, Q. Tu, Q. Yue and Y. Kang, *Adv. Funct. Mater.*, 2021, 2107182.
70 P. Zhu, C. Xia, C.-Y. Liu, K. Jiang, G. Gao, X. Zhang, Y. Xia, Y. Lei, H. N. Alshareef, T. P. Senftle and H. Wang, *Proc. Natl. Acad. Sci. U. S. A.*, 2021, **118**, e2010868118.
71 C.-J. Peng, G. Zeng, D.-D. Ma, C. Cao, S. Zhou, X.-T. Wu and Q.-L. Zhu, *ACS Appl. Mater. Interfaces*, 2021, **13**, 20589–20597.
72 Y. Wang, X. Zhu and Y. Li, *J. Phys. Chem. Lett.*, 2019, **10**, 4663–4667.
73 Q. Wang, C. Zhu, C. Wu and H. Yu, *Electrochim. Acta*, 2019, **319**, 138–147.
74 F. Bienen, A. Löwe, J. Hildebrand, S. Hertle, D. Schonvogel, D. Kopljar, N. Wagner, E. Klemm and K. A. Friedrich, *J. Energy Chem.*, 2021, **62**, 367–376.
75 Y. Qiu, J. Du, C. Dai, W. Dong and C. Tao, *J. Electrochem. Soc.*, 2018, **165**, H594–H600.
76 P. F. Liu, M. Y. Zu, L. R. Zheng and H. G. Yang, *Chem. Commun.*, 2019, **55**, 12392–12395.
77 Y.-R. Wang, R.-X. Yang, Y. Chen, G.-K. Gao, Y.-J. Wang, S.-L. Li and Y.-Q. Lan, *Sci. Bull.*, 2020, **65**, 1635–1642.
78 E. Bertin, S. Garbarino, C. Roy, S. Kazemi and D. Guay, *J. CO2 Util.*, 2017, **19**, 276–283.
79 Z. Tao, C. L. Rooney, Y. Liang and H. Wang, *J. Am. Chem. Soc.*, 2021, **143**, 19630–19642.
80 C. L. Rooney, Y. Wu, Z. Tao and H. Wang, *J. Am. Chem. Soc.*, 2021, **143**, 19983–19991.
81 Y. Zhao, J. Liang, C. Wang, J. Ma and G. G. Wallace, *Adv. Energy Mater.*, 2018, **8**, 1702524.
82 W. Ni, Y. Gao, Y. Lin, C. Ma, X. Guo, S. Wang and S. Zhang, *ACS Catal.*, 2021, **11**, 5212–5221.
83 X. Zu, X. Li, W. Liu, Y. Sun, J. Xu, T. Yao, W. Yan, S. Gao, C. Wang, S. Wei and Y. Xie, *Adv. Mater.*, 2019, **31**, 1808135.
84 W. Luc, C. Collins, S. Wang, H. Xin, K. He, Y. Kang and F. Jiao, *J. Am. Chem. Soc.*, 2017, **139**, 1885–1893.
85 X. Bai, W. Chen, C. Zhao, S. Li, Y. Song, R. Ge, W. Wei and Y. Sun, *Angew. Chem., Int. Ed.*, 2017, **56**, 12219–12223.
86 S. Yan, C. Peng, C. Yang, Y. Chen, J. Zhang, A. Guan, X. Lv, H. Wang, Z. Wang, T.-K. Sham, Q. Han and G. Zheng, *Angew. Chem., Int. Ed.*, 2021, **60**, 25741–25745.
87 D. Li, L. Huang, Y. Tian, T. Liu, L. Zhen and Y. Feng, *Appl. Catal., B*, 2021, **292**, 120119.
88 X. Zhang, F. Li, Y. Zhang, A. M. Bond and J. Zhang, *J. Mater. Chem. A*, 2018, **6**, 7851–7858.
89 C. Liu, Z. Ma, M. Cui, Z. Zhang, X. Zhang, D. Su, C. B. Murray, J. X. Wang and S. Zhang, *Nano Lett.*, 2018, **18**, 7870–7875.
90 H. Hwang, T. Kwon, H. Y. Kim, J. Park, A. Oh, B. Kim, H. Baik, S. H. Joo and K. Lee, *Small*, 2018, **14**, 1702353.
91 F. Gao, Y. Zhang, H. You, Z. Li, B. Zou and Y. Du, *Small*, 2021, **17**, 2101428.
92 S. Yin, Z. Wang, S. Liu, S. Jiao, W. Tian, Y. Xu, X. Li, L. Wang and H. Wang, *Nanoscale*, 2021, **13**, 3208–3213.
93 D.-H. Zhuo, Q.-S. Chen, X.-H. Zhao, Y.-L. Jiang, J. Lu, Z.-N. Xu and G.-C. Guo, *J. Mater. Chem. C*, 2021, **9**, 7900–7904.
94 Y. Li, H. Yang, X. Hu, H. Tian, M. Gao, D. Zhang, Z. Li and D. Yang, *ChemElectroChem*, 2019, **6**, 3782–3790.
95 Q. Li, Y. Zhang, X. Zhang, H. Wang, Q. Li, J. Sheng, J. Yi, Y. Liu and J. Zhang, *Ind. Eng. Chem. Res.*, 2020, **59**, 6806–6814.